sustainability

MDPI

Article

Numerical Simulation Investigation of Wind Field Characteristics and Acceleration Effects over V-Shaped Hills

Jianfeng Yao [1,2,3], Zhibin Tu [1] and Haiwei Xu [2,*]

[1] Nanxun Innovation Institute, Zhejiang University of Water Resources and Electric Power, Hangzhou 310018, China; yaojf@zjweu.edu.cn (J.Y.); tuzb@zju.edu.cn (Z.T.)
[2] College of Civil Engineering and Architecture, Zhejiang University, Hangzhou 310058, China
[3] Energy Engineering Group Zhejiang Power Design Institute Co., Ltd., Hangzhou 310012, China
* Correspondence: haiweix@zju.edu.cn; Tel.: +86-0571-86929012

Abstract: Wind energy resources play an important role in sustainable development, and the accelerating effect of wind has been found in V-shaped hills, which informs the siting of wind turbines in this type of terrain. The wind field around the V-shaped hill was simulated using the CFD method. The impact of wind angle, hill pinch angle, and the distance between the hills on the wind field around the V-shaped hill was investigated. Wind acceleration effects at specific locations were studied and analyzed, and these findings were compared with established codes. It was observed that the wind speed at the hill's top under each wind angle is significantly higher compared to other areas. Additionally, the acceleration ratio at the top generally exhibits a decreasing trend with increasing height. If the wind angle is 15° and the pinch angle is greater than or equal to 15°, or if the distance between the hills is less than or equal to 50 m, the wake zone will gradually transition from two to one. The distance between the hills minimally affects the acceleration ratio at the mid-height and top of the hill. Several codes exhibit inconsistency in specifying acceleration effects in hilly terrain. The findings in this paper align most closely with the American code at the base of the hill. At the hill's top, the American code is the lowest above 100 m, while the Chinese code is the highest below 100 m. The findings in this paper fall between those of the Japanese and Australian codes. The formulas for the variation in wind speed acceleration ratio at typical locations with respect to height and the angle between the hills are provided.

Keywords: hilly terrain; speed-up; wind field calculation; CFD; wind energy

check for updates

Citation: Yao, J.; Tu, Z.; Xu, H. Numerical Simulation Investigation of Wind Field Characteristics and Acceleration Effects over V-Shaped Hills. *Sustainability* **2024**, *16*, 9274. https://doi.org/10.3390/su16219274

Academic Editor: Shuhua Fang

Received: 11 October 2024
Revised: 21 October 2024
Accepted: 23 October 2024
Published: 25 October 2024

Copyright: © 2024 by the authors. Licensee MDPI, Basel, Switzerland. This article is an open access article distributed under the terms and conditions of the Creative Commons Attribution (CC BY) license (https://creativecommons.org/licenses/by/4.0/).

1. Introduction

New energy sources, such as solar and wind power, are currently under development, with a significant number of these energy devices being constructed in hilly terrains. The safety of these energy devices and the integrity of the power transmission system are directly linked to the boundary layer wind field. Wind-induced damage to photovoltaic plants, wind turbines, and transmission tower-line systems is a frequent occurrence. Nevertheless, the diverse topographic variations in hilly terrain significantly influence the wind field, particularly causing a substantial increase in mean wind speed within the local area, leading to the formation of micro-terrain meteorology. In addition, the issue of siting for these new sources of energy is also very prominent, especially the siting of wind turbines, which requires a balance between safety and efficiency. However, the current design codes for hilly terrain wind fields do not universally apply to all hilly terrains, thus highlighting the significance of studying hilly terrain wind fields.

It is necessary to utilize reasonable and effective research means for successfully carrying out research on the characteristics of hilly terrain wind fields. At present, there are three main research methods for hilly terrain wind fields: field measurement, wind tunnel tests, and numerical simulation. Field measurement can obtain the most direct

and effective data, but it is time-consuming and labor-intensive, can only obtain random data, and the observation points are very limited [1]; the wind tunnel test can simulate the atmospheric wind environment, but it is affected by the boundary effect and similarity criterion [2]; numerical simulation can reconstruct the wind field through computational fluid dynamics or mathematically modeling the physical mechanism [3]. Utilizing these methods, researchers have studied the regular isolated hill, multiple hills, and real hilly terrain accordingly. The research on the wind field of an isolated hill is relatively early. Jackson and Hunt [4] used a combination of theoretical and numerical calculations to first propose an analytical algorithm of acceleration effect applicable to two-dimensional smooth low hills and verified it with wind tunnel tests, but only the maximum acceleration ratio at the top of the mountain can be calculated. A series of two-dimensional shaped wind tunnel tests were conducted by Neff and Meroney [5], where the effects of hill shape and surface roughness on hilly wind field characteristics were investigated. The results of the study concluded that the effect of hill shape on wind field characteristics is the first dominant factor. Ishihara et al. [6] used a wind tunnel test to study the mean wind speed and turbulence distribution of a three-dimensional hill at the top, hillside, and foot of the hill, and the results showed that the wind speed near the foot of the windward slope decreased, but the wind speed at the top and the hillside increased significantly, and the wind speed at the top increased by 50% to 60%. Lubitz et al. [7] investigated the effects of different wind angles on the wind field of a hill through wind tunnel tests and compared them with the field wind speed data to reveal the effects of the incoming wind direction on the acceleration ratio of the wind speed on the mountain slopes. Li Zhengliang et al. [8] conducted numerical simulations for a three-dimensional axisymmetric hilly terrain wind field and investigated the influence of factors such as hill height, slope, and geomorphology type on the wind acceleration effect and proposed a correction formula for the wind speed at the top of the hill. Song Jialing et al. [9] compared numerical simulations with wind tunnel testing at a bridge site in a Y-shaped valley. They identified the k-model as the most accurate among three RANS turbulence models, proposing practical equations for predicting wind deflection and the use of a modified terrain coefficient for secure wind speed predictions. Shortcomings in national bridge design codes for mountainous areas are also highlighted.

Multi-hill terrain wind fields are more complex than the isolated hilly terrain wind fields. The wind field characteristics of two-dimensional continuous hills were studied by Miller and Davenport [10], who found that the acceleration effect will be reduced in composite terrain compared to isolated hill terrain. Carpenter and Locke [11] examined two-dimensional hills for atmospheric boundary layer wind tunnel tests and came to similar conclusions as Miller and Davenport, concluding that wind speeds are greatest at isolated hills. Breuer et al. [12] used wind tunnel tests and numerical simulations to study the flow around a two-dimensional periodic hill, solved the physical mechanism of periodic slope flow, and extended the range of Reynolds numbers in previous studies. Li Zhengliang et al. [13] conducted a wind tunnel test on a three-dimensional hill under sheltered conditions to investigate the effects of the distance between hills, the slope of the applied disturbed hill, and the height of the applied disturbed hill on the distribution patterns of the mean and pulsating winds at each location of the disturbed hill. The results show that the maximum acceleration ratio of the near-ground mean wind speed at the top of the hill decreases rapidly with the increase in the spacing distance; the acceleration ratio at the top of the hill increases rapidly with the increase in the slope of the sheltered hill and finally stabilizes. Shen et al. [14] conducted a wind tunnel test study for an isolated hill and two adjacent hill wind fields to investigate the effects of hill slope and hill distance on the downwind mean wind speed. Zhenghao Li [15] and Wenjuan Lou et al. [16] introduced the important factor of the length of the mountain range on the basis of the axisymmetric hill model and investigated the influences of the top distance, the slope of the mountain range, and the length of the mountain range on the acceleration effect of the wind field in the passes and canyons based on the wind tunnel test and the numerical simulation of CFD.

For some specific projects, real complex terrains have also been studied. Andrew et al. [17] used field measurements to observe the wind field at Niwot Ridge, located in the Rocky Mountains of the U.S.A., for a period of 4 months and summarized the wind field patterns of isolated hills, multiple hills, canyons, and other hilly terrains, which provided a test standard for subsequent studies. Bai Hua et al. [18] conducted a wind tunnel test to characterize the wind field for complex terrain at the river valley where the Sanshui River Bridge is located and concluded that there is no obvious canyon wind effect at the bridge site. Jubayer and Hangan [19] used a hybrid method of numerical simulation and wind tunnel test to evaluate the wind field conditions in real complex terrain, where numerical simulations provide the in-flow conditions for wind tunnel tests, and acceleration effect studies were carried out for the locations of the proposed transmission towers in the specified real terrain. Yu et al. [20] conducted field measurements of wind speed in a deep canyon in the bridge area of the Dadu River Bridge to determine the effect of local topography on the mean wind characteristics. Yang Qingshan et al. [21] further considered the influence of incoming flow and used large eddy simulation to study the influence of upstream turbulence intensity and wind shear coefficient (ground roughness index) on a three-dimensional complex hilly terrain wind field, which assisted in the micro-siting of wind farms, as well as the structural design of wind turbines. Xu Cheng et al. [22] introduced the RANS-VMM method, which combines on-site wind measurements with RANS simulations to improve wind resource assessment accuracy in complex terrains. Results show significant enhancement in assessing wind resources in such challenging environments.

It can be seen from the above review that there are many studies on hilly terrain wind fields, but none of them are on V-shaped hilly terrain wind fields. Due to the influence of topography, the hilly terrain wind field becomes more complicated, and the V-shaped hill is a typical hilly terrain. Considering the lack of clear provisions in the current code for hilly terrain wind fields, this paper carries out numerical simulations of V-shaped hills and investigates the influence of the wind angle, angle of the hill, and the spacing of the hills on the hilly terrain wind field and studies the accelerating effect of the hilly terrain wind field in relation to the flat terrain wind field and finally compares the results of this study with the codes of various countries. The results can provide design references for similar hilly terrain wind fields.

2. Materials and Methods

The analysis of typical hill types on satellite maps, particularly in Figure 1 (the red line represents the ridgeline), reveals that V-shaped hills are more prevalent, while the shapes of hill contours exhibit variation. Among the common hill model contours are the cosine shape, Gaussian shape, bell shape, triangle, etc. However, each model contour is unable to precisely replicate the actual hill shape, thus mitigating the necessity of excessively pursuing the shape's accuracy.



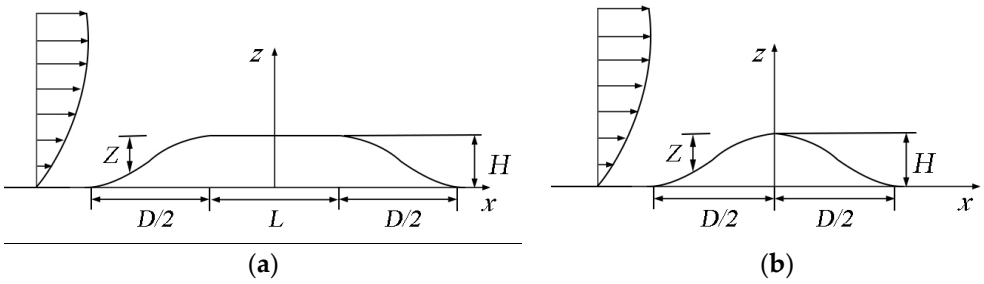
Figure 1. Typical V-shaped hill on satellite view.

After an extensive review of prior research, the decision to employ the cosine-shaped hill model directly in this study was made, and the corresponding diagram of the hill and

its cross-section is depicted in Figure 2. Equation (1) represents the two-dimensional hill contour expression.

$$z = \begin{cases} H\cos^2\left(\pi\frac{x}{D}\right) & x < \frac{D}{2} \\ 0 & x \geq \frac{D}{2} \end{cases} \quad (1)$$

where H is the height of the hill, D is the diameter of the hill. The height of the hill in this study H is 100 m, the diameter D is 300 m, and the length of the range L is 300 m.

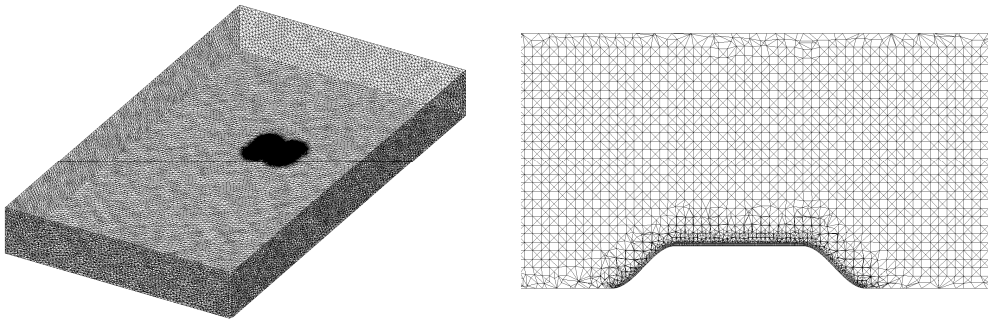


(**a**) (**b**)

Figure 2. Diagram of the hill. (**a**) Longitudinal section of the hill. (**b**) Cross-section of the hill.

Computational Fluid Dynamics (CFD), a primary research method for wind load characterization, offers advantages such as cost-effectiveness, short cycle time, accurate depiction of the flow field environment, and cost efficiency compared to physical wind tunnel testing. To ensure full development of the fluid within the computational domain, the height is set at 600 m, while the width and length are determined by factors such as 3 times the length of the model in front of the hill, 5 times the length of the model behind the hill, and a width of 5 times the model's width, maintaining an obstruction ratio of less than 3% for all models. The figure provides details on the incoming flow direction and defines the x, y, and z coordinates, where z represents the altitude direction, x denotes the incoming wind flow direction, and y indicates the crosswind direction.

The model's surface mesh was constructed using an unstructured quadrilateral mesh and refined at the hill's surface with a horizontal dimension of 5 m. The mesh size was expanded outward from the hill's surface by defining the size function, incorporating a diffusion rate of 1.05 and a maximum horizontal dimension of 40 m. The computational domain is discretized using a hybrid hexahedral mesh. To ensure near-surface computation accuracy, the height of the initial grid layer must consider factors such as the wall function used and surface roughness. For general simulation of the hill terrain wind field, the height of the initial grid layer can be set at 1 m, with vertical growth adjusted proportionally; in this study, the vertical growth rate is 1.1. The total number of grids for each case ranges between 1.5 and 4 million. The computational domain model and basin grid are depicted in Figure 3.



(**a**) (**b**)

Figure 3. Diagram of mesh. (**a**) Mesh of wind field. (**b**) Mesh of hill surface.

The Realizable k−ε model, widely recognized for simulating the atmospheric boundary layer, was adopted as the turbulence model. The inlet, outlet, lateral, and upper

surfaces of the flow field were designated as the velocity inlet, pressure outlet, and symmetry surface, as indicated in Table 1. The surface of the hill and the surrounding flat terrain were designated as the wall surfaces. The simulation employed the non-equilibrium wall function, utilizing a second-order numerical discretization format. The roughness of the hill's ground surface was set to 1 m, while the flat ground exhibited a roughness of 0 m.

Table 1. The settings of boundary conditions.

Location	Boundary Condition
Inflow Surface	Velocity Inlet
Outflow Surface	Pressure Outlet
Side	Symmetry
Top Surface	Symmetry
Ground	Wall
Hill	Wall

The mean wind speed and turbulence profiles of the incoming flow were selected according to the 2012 version of the load specification [23], and the geomorphological category is B, $\alpha = 0.15$, and the wind speed (u_{10}) is set to be 30 m/s for the height of 10 m. The mean wind speed (u) and turbulence (I_u) profiles are as follows:

$$u = u_{10}\left(\frac{z}{10}\right)^{0.15} \tag{2}$$

$$I_u = 0.15\left(\frac{z}{10}\right)^{-0.15} \tag{3}$$

The mean wind speed, turbulent kinetic energy, and turbulent dissipation rate at the inlet were programmed to be input through the user-defined function, where the turbulent kinetic energy expression and the dissipation rate expression are

$$k(z) = 0.5[I(z)u(z)]^2 \tag{4}$$

$$\varepsilon = \frac{4C_\mu^{0.75}k(z)^{1/3}}{KL_u} \tag{5}$$

where C_μ generally takes the value of 0.09 and $K = 0.42$, $I_u(z)$ represents the degree of turbulence at the height of z, and L_u is the turbulence integration scale. Due to the lack of corresponding formulas for these two parameters in the Chinese code [23], the formulas in the Japanese code [24] are used here:

$$I(Z) = \begin{cases} 0.1(\frac{Z}{Z_g})^{-\alpha-0.05} 5 \le Z \le Z_g \\ 0.1(\frac{Z_b}{Z_g})^{-\alpha-0.05} Z \le Z_b \end{cases} \tag{6}$$

$$l = \begin{cases} 100(\frac{Z}{300})^{0.5} \ldots 30\text{m} \le Z \le Z_g \\ 100 \ldots Z \le 30\text{m} \end{cases} \tag{7}$$

where Z_g is the height of the gradient winds, and $Z_b = 5$ m in the category B.

Three representative locations were analyzed in this study: the foothills, the mid-height of the hill, and the hilltop. The selection of these three locations is depicted in Figure 4. The measuring points at the foothills were labeled as 1, 7, 11, 27, 31, and 37; at the mid-height of the hill as 4, 18, and 20; and at the hilltop as 9, 19, and 29. The calculated working conditions are presented in Table 2.

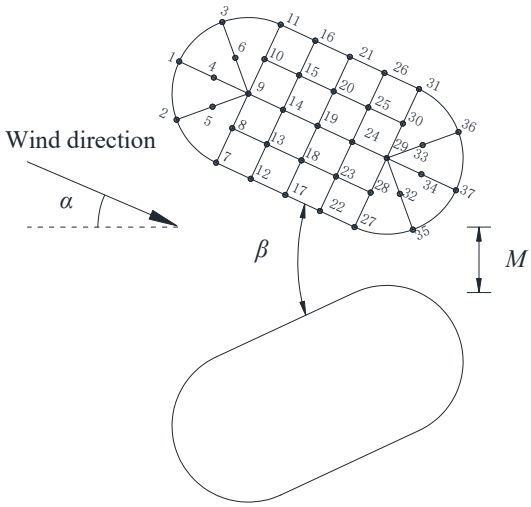


Figure 4. Layout of measurement points.

Table 2. Calculated working conditions.

No.	α	β	M
1	0°~45°@15°	30°	0
2	15°	0°~45°@15°	0
3	15°	30°	0~2D@0.5D

To better represent the variation in wind speed at different locations of the V-shaped hill, the acceleration ratio is defined as

$$S = \frac{u(Z)}{u_0(Z)} \tag{8}$$

where $u(Z)$ denotes the wind speed at height z from the hill surface and $u_0(Z)$ denotes the wind speed at height z from the ground.

3. Validation of Numerical Simulation Accuracy

The wind velocity profile at the measurement point on the hill's frontal location was extracted and compared with the incoming wind profile. The results, depicted in Figure 5, demonstrate the accurate application of the defined wind profile to the hill using this inlet boundary condition, indicating the numerical simulation's robust self-sustainability.

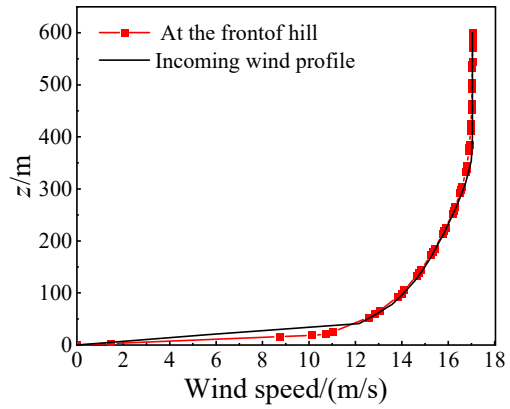


Figure 5. Self-holding validation.

To verify grid-independence, three different grid sizes—2.3 million, 3.7 million, and 5.5 million—were chosen for the numerical simulations. The results were then compared

with the wind tunnel test results of Lou Wenjuan [16], depicted in Figure 6. As observed in Figure 4, the three different grid sizes align well with the wind tunnel test values. This not only substantiates the accuracy of the numerical simulation but also indicates that, at this stage, the results and the number of grids do not significantly impact the subsequent selection of approximately 2 million mesh elements.

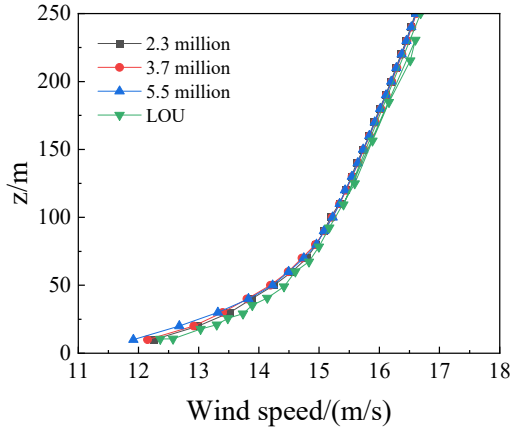


Figure 6. Mesh sensitivity test.

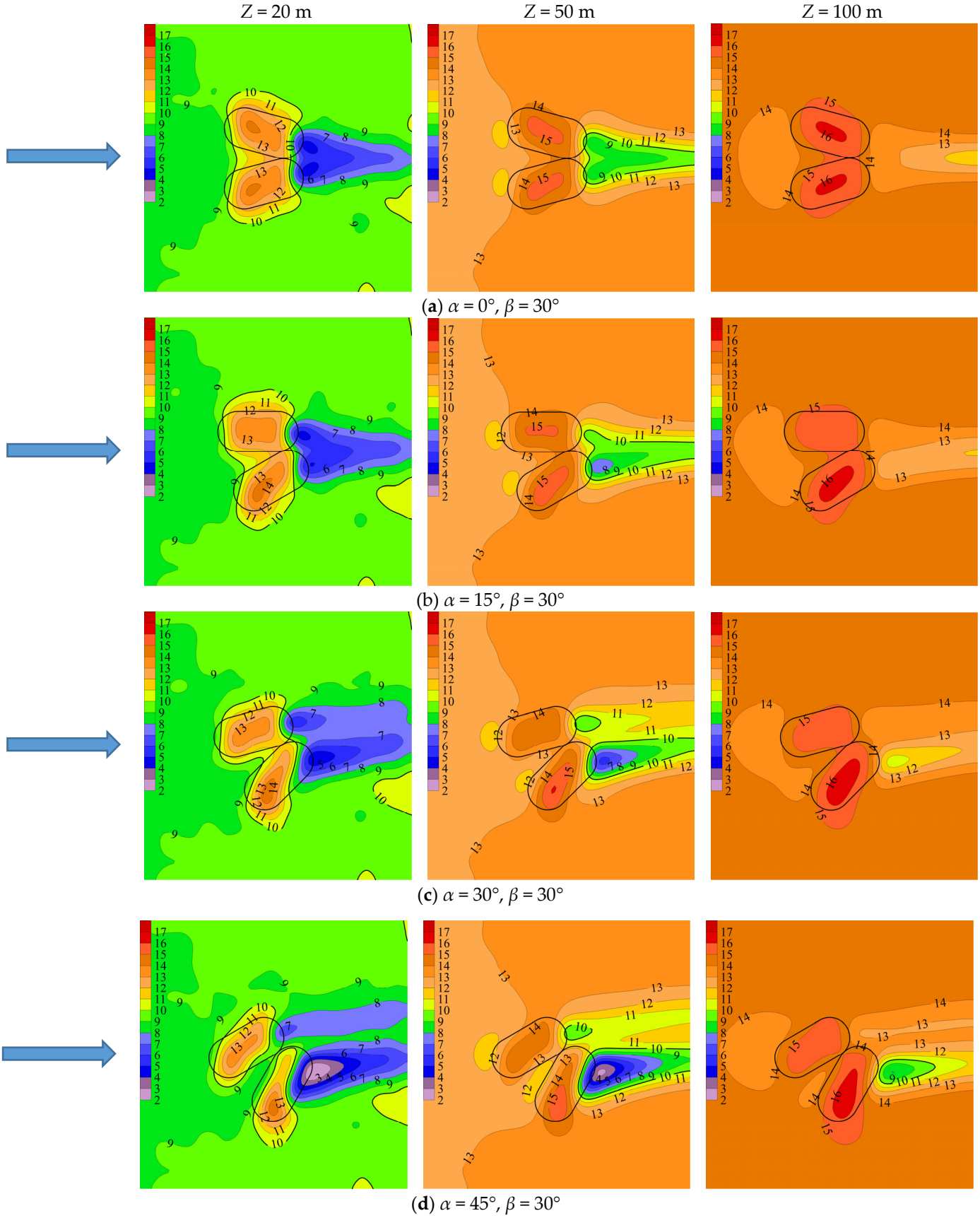
4. Results and Discussion

4.1. The Influence of Wind Direction

To explore the impact of wind direction on the V-shaped hill, a hill with a pinch angle of 30° was chosen for the study. The wind direction ranged from 0° to 45° at 15° intervals. Figure 7 illustrates the wind speeds at varying distances from the ground (hill surface) for a V-shaped hill with a 30° hill pinch angle, considering different wind direction angles: 0°, 15°, 30°, and 45°. At the hilltop, the wind speed surpasses that of other regions for all wind direction angles. Furthermore, a consistent wake region forms behind the V-shaped hill, irrespective of the wind direction angle. As the wind direction angle equals or exceeds 10°, the wake region gradually separates with increasing wind direction angle.

Based on the calculations derived from Equation (2), the wind speeds at heights of 20 m, 50 m, and 100 m above the ground are 11.1 m/s, 12.7 m/s, and 14.1 m/s, respectively. Various heights demonstrate different degrees of acceleration zones near the hill's top. Particularly, at 20 m in height, the windward side of the V-shaped hill encounters a localized deceleration zone under various wind angles, which diminishes with increasing height. Moreover, at the same height, the maximum wind speed on the V-shaped hill gradually concentrates at the peak of hill 2 as the wind angle rises, resulting in an overall increase in the maximum wind speed. Additionally, as the wind angle increases, the wind speed regions of hill 1 and hill 2 tend to become increasingly independent of each other.

The wind acceleration ratios at the foot of the hill at different wind angles are shown in Figure 8, which illustrates the significant variation in acceleration ratios for measurement points 1 and 31 as the wind angle changes. These acceleration ratios all increase with the wind direction angle. Measurement point 37 has negligible impact on the acceleration ratio beyond a height of 150 m. The magnitude of acceleration ratios for measurement points 7, 11, 27, and 31 varies significantly under different wind angles, all decreasing with increasing wind angle. Among them, the acceleration ratio of measurement point 7 increases with the increase of height, and tends to 1 at 200 m, indicating that the acceleration ratio at this height is no longer affected by the topography and wind angle. The acceleration ratio of measurement point 11 increases with height at wind angles greater than 30°, and decreases with height at angles less than 30°. At a wind angle of 0°, the acceleration ratio of measurement point 31 remains relatively constant with increasing height. The maximum acceleration ratio is observed at measurement point 11, with a value exceeding 1.2.



(**a**) $\alpha = 0°$, $\beta = 30°$

(**b**) $\alpha = 15°$, $\beta = 30°$

(**c**) $\alpha = 30°$, $\beta = 30°$

(**d**) $\alpha = 45°$, $\beta = 30°$

Figure 7. Contour plots of wind speed at various heights for different wind angles.

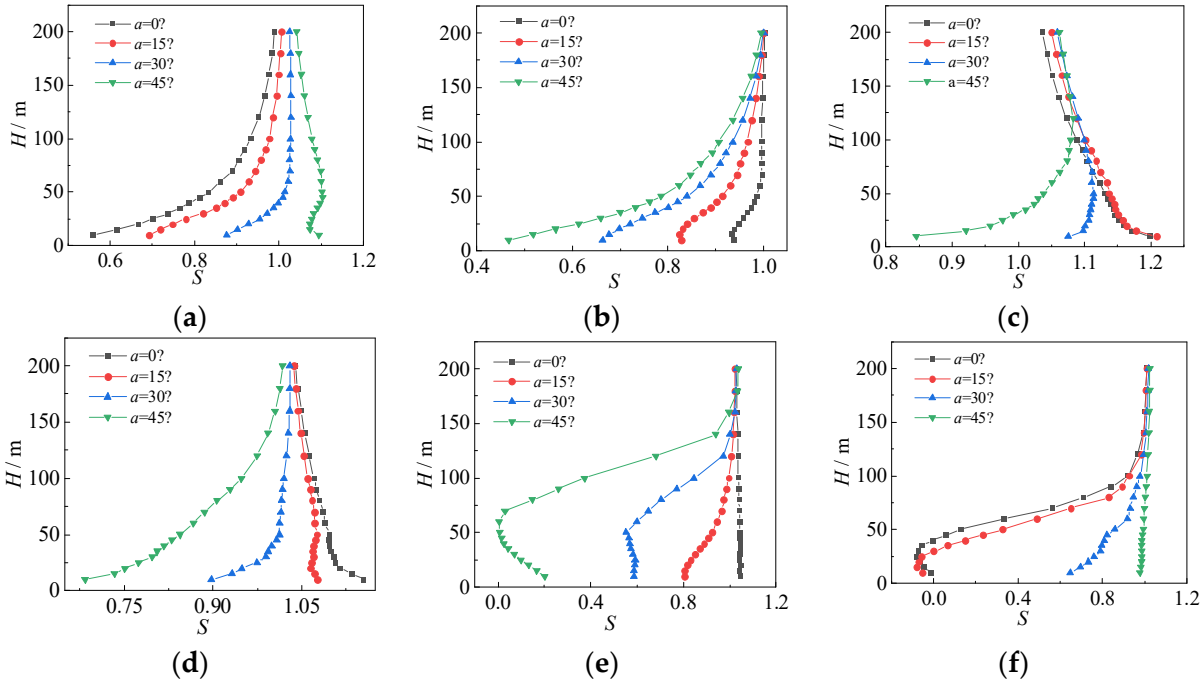


Figure 8. Wind acceleration ratios at the foothill for $\beta = 30°$. (**a**) Point 1. (**b**) Point 7. (**c**) Point 11. (**d**) Point 27. (**e**) Point 31. (**f**) Point 37.

The acceleration ratios at the midpoint of the hill are depicted in Figure 9. It is evident that the acceleration ratio of measurement point 4 increases with the wind angle, while the acceleration ratios of measurement points 18 and 20 decrease with the wind angle. For measurement points 18 and 20 at heights exceeding 150 m, the acceleration ratio converges to a constant value across different wind angles, suggesting minimal influence of the wind angle. The acceleration ratios of measurement points 18 and 20 become more influenced by the wind angle once it surpasses 15°. The maximum acceleration ratio, exceeding 1.5, is observed at measurement point 4.

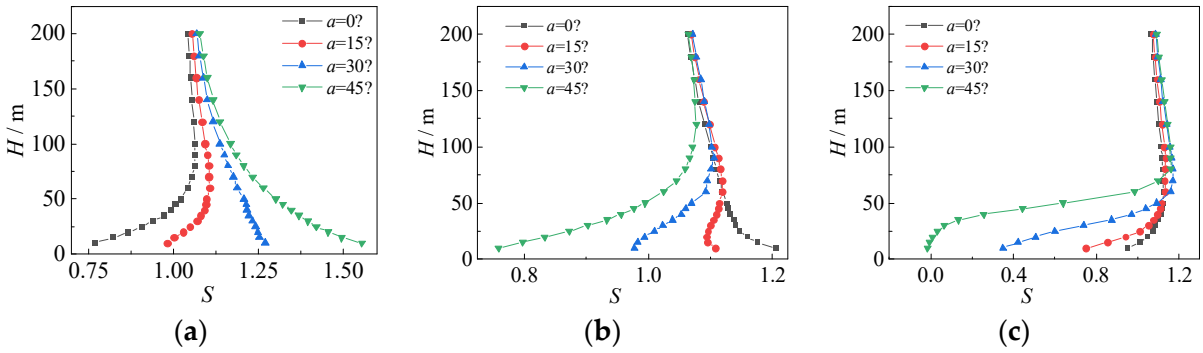


Figure 9. Wind acceleration ratios at the mid-height of the hill for $\beta = 30°$. (**a**) Point 4. (**b**) Point 18. (**c**) Point 20.

The acceleration ratios at the hill's top are illustrated in Figure 10, indicating a general decreasing trend in the acceleration ratios of measurement points 9, 19, and 29 with increasing height. The acceleration effect at measurement point 9 increases with the wind angle, while the acceleration effect at measurement point 29 shows minimal variation with changes in wind angle. The most notable acceleration effect occurs at point 9, reaching a maximum value of nearly 1.9.

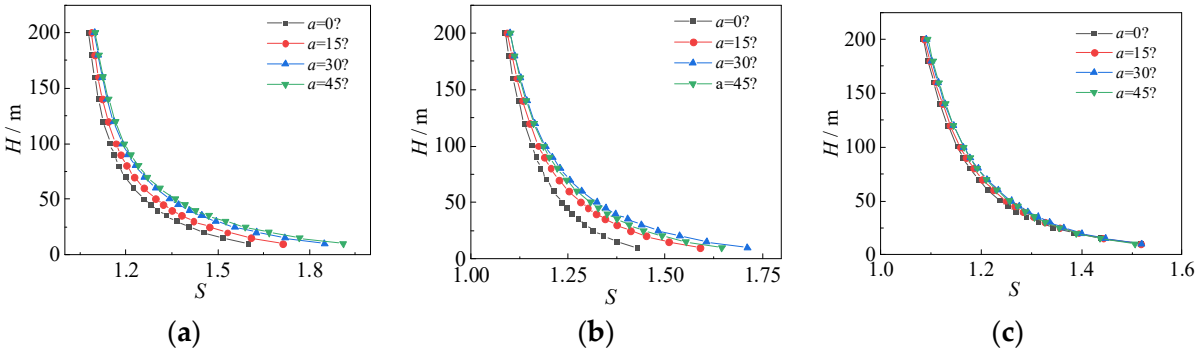


Figure 10. Wind acceleration ratios at the top of the hill for $\beta = 30°$. (**a**) Point 9. (**b**) Point 19. (**c**) Point 29.

4.2. The Influence of Hill Pinch Angle

To investigate the impact of the hill pinch angle on the mean wind field, a wind direction of 15° was selected. Figure 11 illustrates the contour plots of wind speeds at varying distances (20 m, 50 m, and 100 m) from the ground or hill surface, considering different hill pinch angles under a wind direction of 15°. It is evident that the flow field characteristics of the V-shaped hill remain consistent across varying heights and hill pinch angles. Wind speeds at the hill's top are marginally higher than those in other regions for all wind angles. Additionally, the V-shaped hill creates a wake area behind each of the two hills, which gradually merges into one when the hill pinch angle is greater than or equal to 15°. At a hill pinch angle of 15°, the wind acceleration effect of the V-shaped hill is most pronounced at a wind angle of 15°.

Figure 12 illustrates the acceleration of wind speed at the hill's base at a wind angle of 15°. It is evident that the acceleration effect at measurement point 1 exhibits minimal variation with changes in wind angle and increases proportionally with height, approaching a value close to 1. The acceleration effect at measurement point 7 intensifies as the wind angle decreases, while the acceleration ratio at measurement point 11 increases with higher wind angles. Additionally, the acceleration effect at measurement point 37 notably varies within the height range of 50 m–100 m, and the acceleration ratio tends to stabilize after surpassing a height of 150 m. The maximum acceleration ratio, approximately 1.2, is observed at measurement point 11 when the hill pinch angle is 45°.

Figure 13 displays the wind speed acceleration at mid-height of the hill at a wind angle of 15°. It indicates that the hill pinch angles have minimal influence on the acceleration effect at measuring point 4. The acceleration ratio increases with height and stabilizes beyond a certain distance. The acceleration at measurement point 18 is intricate; however, beyond 50 m, its acceleration effect rises as the hill pinch angle decreases. Measurement point 20 exhibits minimal impact on the acceleration effect at all hill pinch angles and diminishes with increasing height. However, at a hill pinch angle of 45° and a height of less than 50 m, the acceleration effect deviates from the other hill pinch angles, with the acceleration ratio increasing as height increases. The maximum acceleration ratio, reaching a value close to 1.2, is observed at measurement point 20.

Figure 14 illustrates the wind speed acceleration at the hill's top at a wind angle of 15°. It indicates a decreasing trend in the acceleration ratios of measurement points 9, 19, and 29 with increasing height. The acceleration effect at points 9 and 29 exhibits minimal variation with the hill pinch angle, whereas point 19 demonstrates a substantial difference at a hill pinch angle of 0°. The maximum acceleration ratio, reaching a value close to 1.6, is observed at point 9.

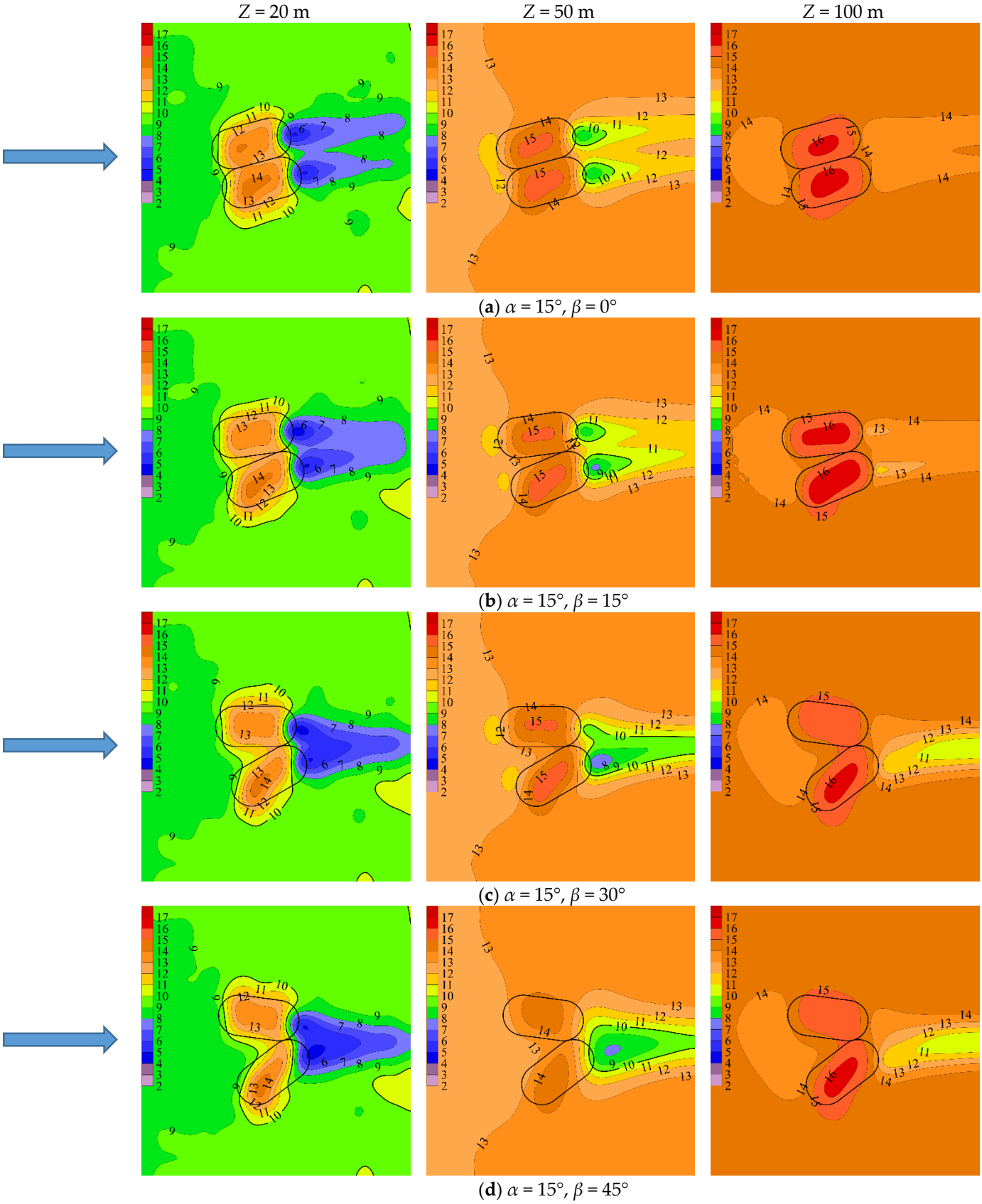


Figure 11. Contour plots of wind speed at various heights for different hill pinch angles.

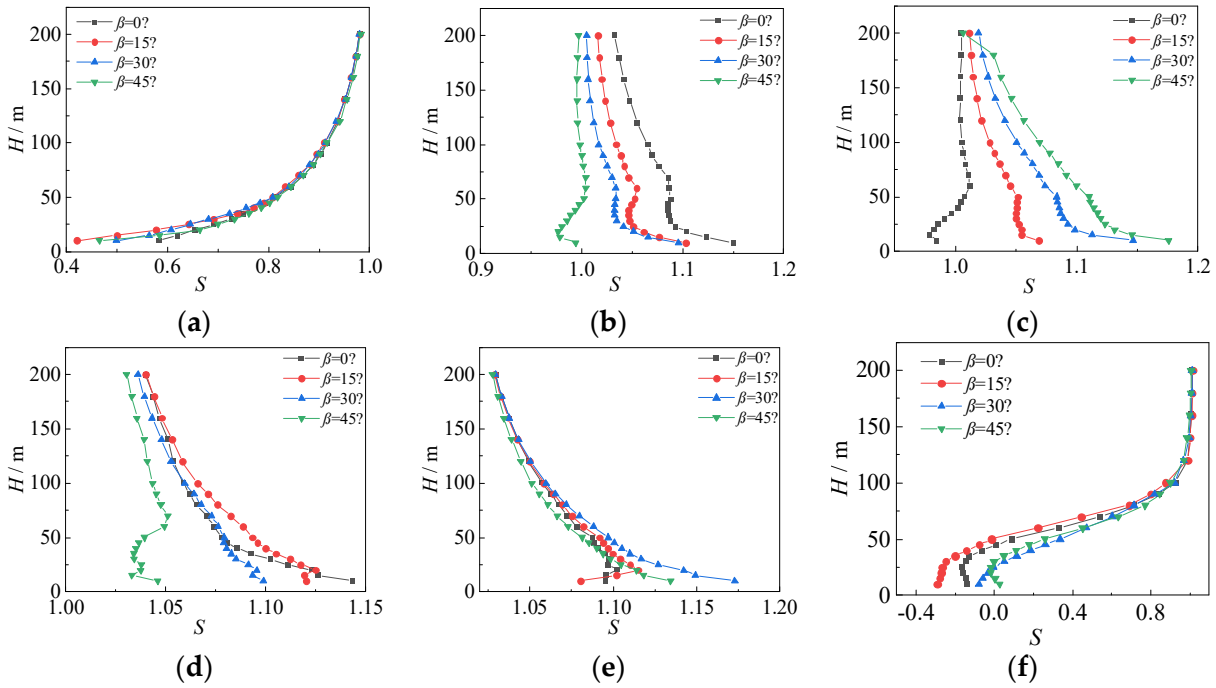


Figure 12. Wind acceleration ratios at the foothill for $\alpha = 30°$. (**a**) Point 1. (**b**) Point 7. (**c**) Point 11. (**d**) Point 37. (**e**) Point 31. (**f**) Point 37.

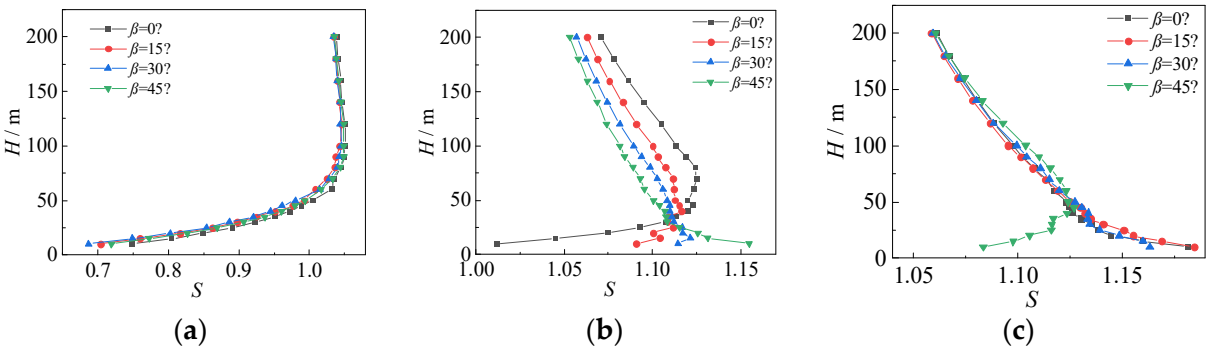


Figure 13. Wind acceleration ratios at the mid-height of the hill for $\alpha = 15°$. (**a**) Point 4. (**b**) Point 18. (**c**) Point 20.

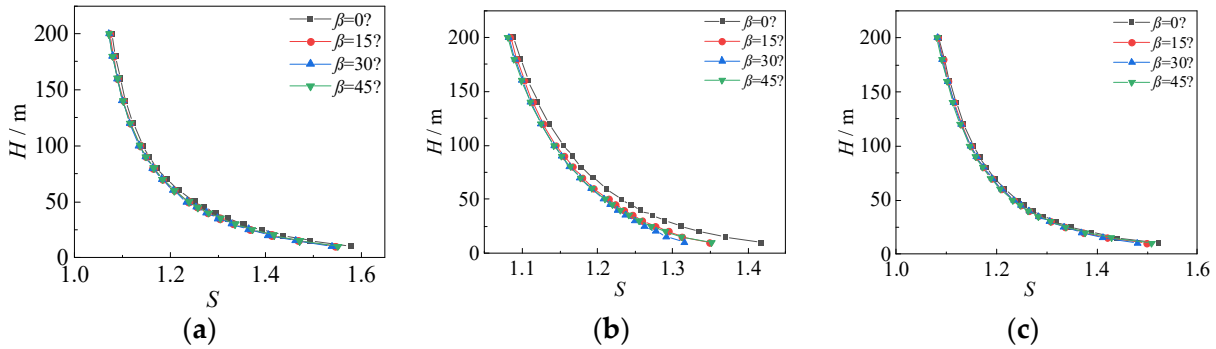


Figure 14. Wind acceleration ratios at the top of the hill for $\alpha = 15°$. (**a**) Point 9. (**b**) Point 19. (**c**) Point 29.

4.3. The Influence of Distance Between Hills

The inter-hill distances within a V-shaped hill significantly impact the wind field of hilly terrain. Consequently, a hill pinch angle of 30° was utilized to examine the wind field of a V-shaped hill with varying inter-hill distances at a 15° wind angle. Figure 15 illustrates

the contour plots of wind speeds at various distances from the ground or hill surface—20 m, 50 m, and 100 m—depicting a V-shaped hill at a wind angle of 15° and a pinch angle of 30°. Observations reveal that the wind speeds at the hill's top are marginally higher compared to the surrounding areas at each inter-hill distance. Additionally, a wake area forms after the two hills, gradually dividing from one to two when the inter-hill distance equals or exceeds 50 m. With increasing height above the ground, the wind speed rises. Furthermore, hill 2 demonstrates a more pronounced sensitivity to inter-hill distances compared to hill 1.

Figure 16 illustrates the acceleration of wind speed at the base of the hill under a wind angle of 15° and a hill pinch angle of 30°. The acceleration impact at measurement points 1, 7, and 31 shows minimal sensitivity to hill spacing, while the acceleration ratios consistently rise with increasing height. Beyond 150 m, the acceleration ratio at measurement point 11 remains essentially unaffected, and the hill spacing demonstrates negligible impact on this ratio. Measurement point 37's acceleration ratio is notably influenced by height. Beyond 150 m, the acceleration effect remains largely unaffected by both height and hill distance, tending towards 1. At M = 0.5 D; the maximum acceleration ratio is observed at measurement point 11.

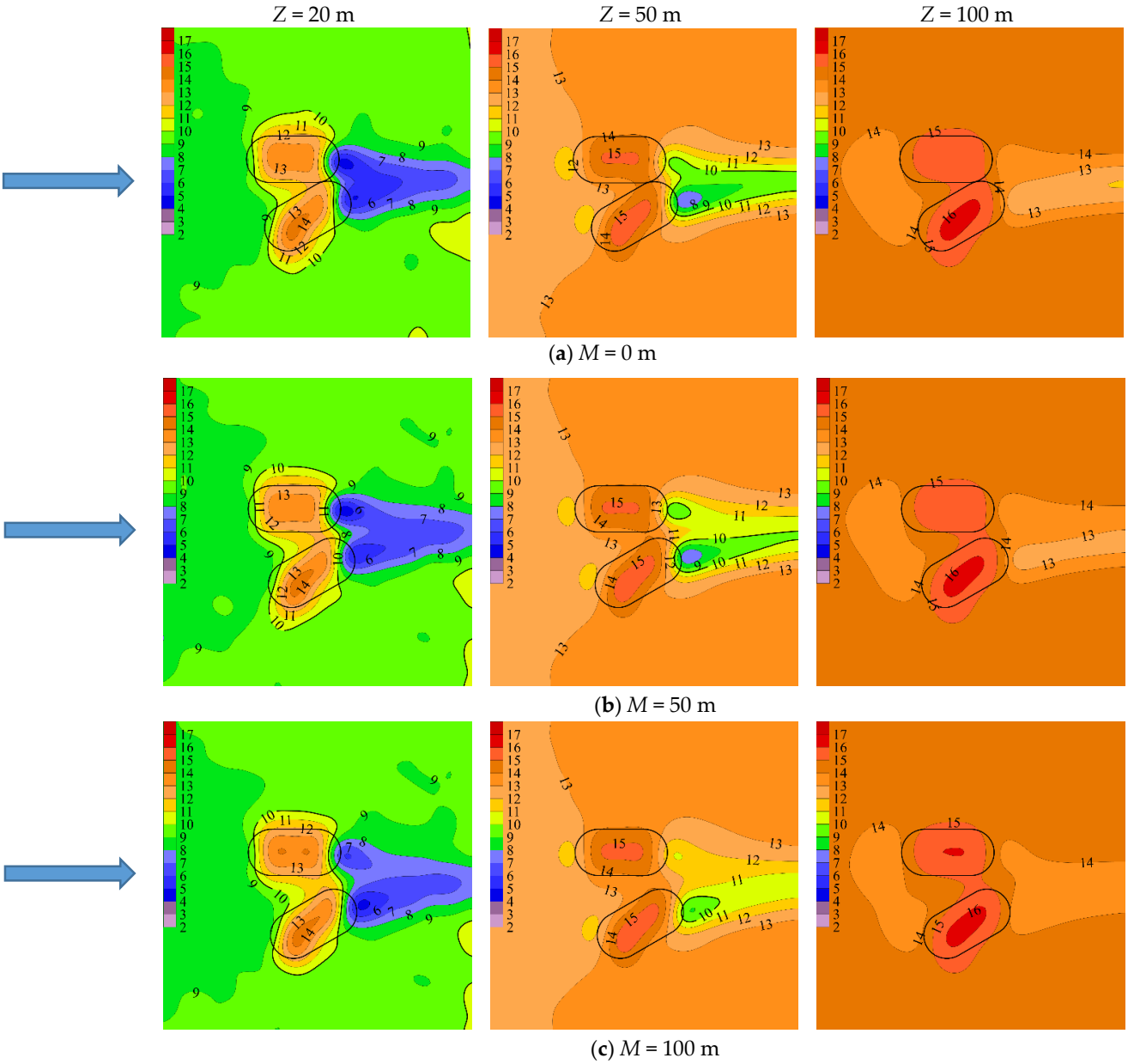
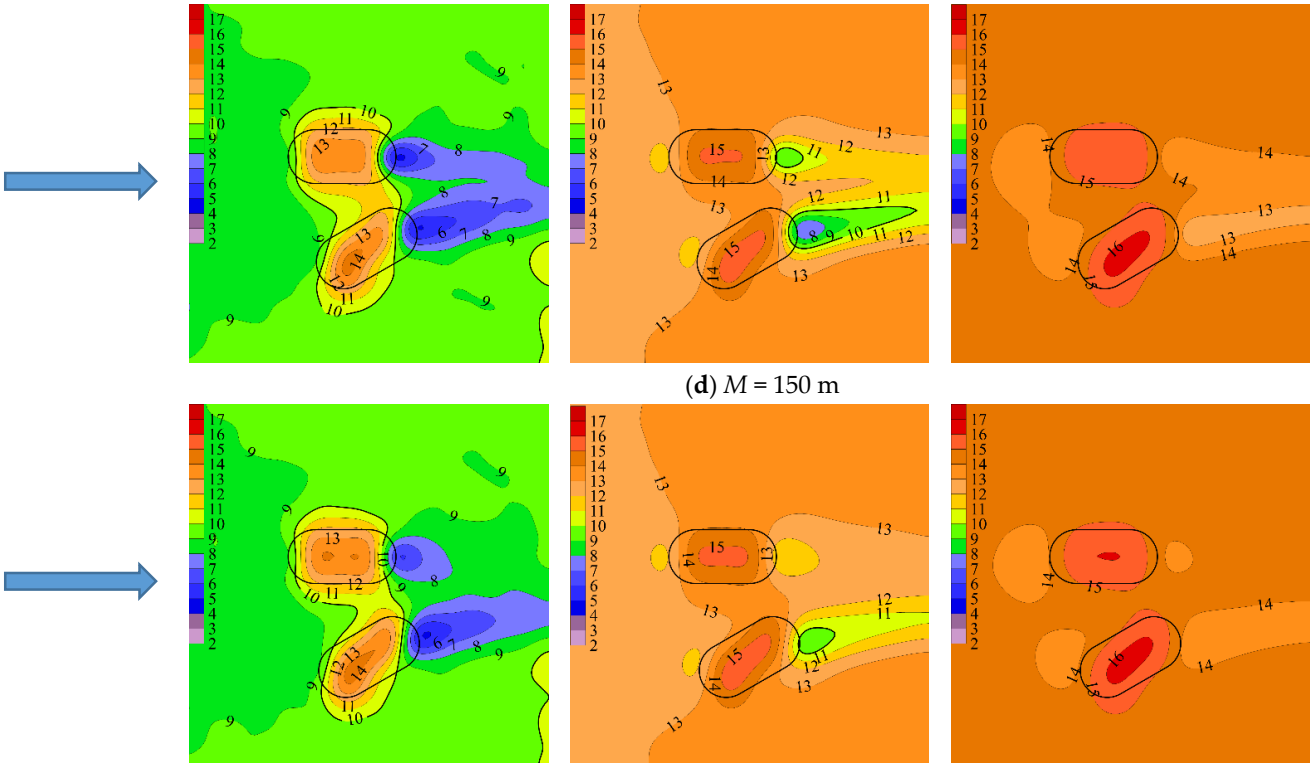


Figure 15. *Cont.*



(**d**) M = 150 m

(**e**) M = 200 m

Figure 15. Contour plots of wind speed at various heights for different distance between hills.

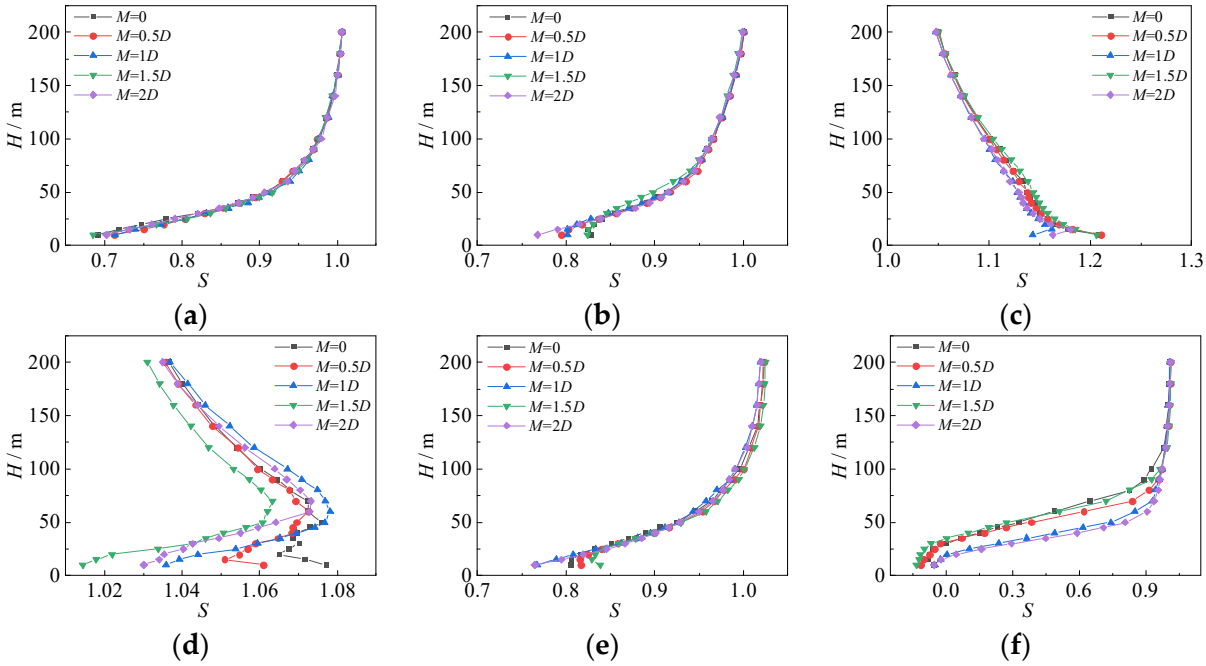


Figure 16. Wind acceleration ratios at the foothill for α = 15° and β = 30°. (**a**) Point 1. (**b**) Point 7. (**c**) Point 11. (**d**) Point 27. (**e**) Point 31. (**f**) Point 37.

Figure 17 depicts the acceleration of wind speed at mid-height of the hill under a wind angle of 15° and a hill pinch angle of 30°. The wind angle minimally affects the acceleration at measurement points 4 and 20. The acceleration ratio initially rises and then declines with increasing height, eventually reaching a point where it has negligible effect. At a hill distance of 1 D, measurement point 18 exhibits a relatively large acceleration ratio

compared to other distances, while at a hill distance of 1.5 D, the acceleration ratio is small. Measurement point 20 demonstrates a maximum acceleration ratio when the hill distance is 1.5 D.

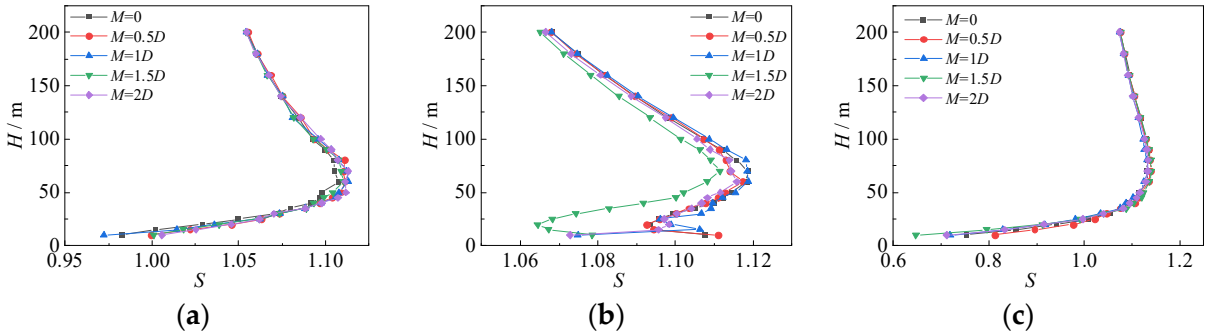


Figure 17. Wind acceleration ratios at the mid-height of the hill for $\alpha = 15°$ and $\beta = 30°$. (**a**) Point 4. (**b**) Point 18. (**c**) Point 20.

Figure 18 illustrates the wind speed acceleration at the hilltop under a wind angle of 15° and a hill pinch angle of 30°. The acceleration effect at measuring points 9 and 19 remains unaffected by the distance between hills, while it diminishes with increasing height. The acceleration ratio of measuring point 29 remains largely unaffected by the distance between hills once the height exceeds 100 m. The maximum acceleration ratio at measuring point 9 occurs when the distance between hills is 0.5 D.

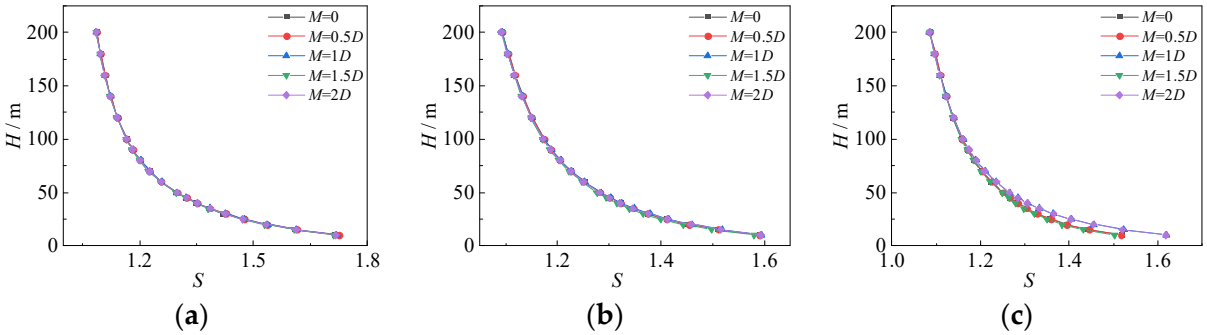


Figure 18. Wind acceleration ratios at the top of the hill for $\alpha = 15°$ and $\beta = 30°$. (**a**) Point 9. (**b**) Point 19. (**c**) Point 29.

4.4. Comparison with Codes

Various national codes address wind fields in hilly terrain. This paper combines common national codes with the specific hill studied, presenting the method for calculating wind speed acceleration ratios in Table 3.

Figure 19 illustrates the acceleration ratios at various locations. It is evident that at the windward foot, the European and Australian codes exceed 1.0, while the Chinese and Japanese codes equal 1.0. The acceleration ratio of the American code is 1.0 at heights exceeding 100 m, and below 1 at heights less than 100 m. Data at measurement point 1 closely align with the American code, whereas data at measurement points 17 and 21 closely align with the European data. In the windward zone, the Japanese code approximates 1.0, while all other national codes exceed 1.0. The US code exhibits the highest acceleration ratio. Data from measurement point 18 closely resemble the Australian code at heights exceeding 50 m, while data from measurement point 20 closely resemble the European code at heights exceeding 10 m. At the hill's top, the acceleration ratio reaches 1.0 at heights exceeding 100 m. Additionally, at the hilltop, all national codes surpass 1.0. The three measurement points in this study closely align at heights exceeding 50 m and are most similar to the Japanese code at heights exceeding 100 m. The data for each country's code are highest at the top of the windward hill.

Table 3. Calculation of wind speed acceleration ratios in various codes.

Code	Calculation Method	Note
GB 50009-2012 [23]	$S = 1 + \kappa \cdot \tan\alpha\left(1 - \frac{z}{2.5H}\right)$	$\tan\alpha$ is the slope; κ is a constant; H is the height of the hill or the slope; and z is the height from the hill surface.
ASCE 7-10 [24]	$S = 1 + \kappa_1\kappa_2\kappa_3$	K_1, K_2, and K_3 are the factors.
EN 2004-1-4 [25]	$S = 1$ for $\phi < 0.05$ $S = 1 + 2s\phi$ for $0.05 < \phi < 0.3$ $S = 1 + 0.6s\phi$ for $\phi > 0.3$	φ is the upstream slope, and s is the orographic location factor.
AS/NZS 1170.2 [26]	$S = 1 + 0.71\left(1 - \frac{\lvert x\rvert}{L_2}\right)\frac{H}{2L_u} > 0.45$	x is the distance from the hill center. L_2 is 4 L_1 at upstream slope and the ridge and 10 L_1 at the downstream side. L_1 is the greater of 0.36 L_u and 0.4 H. L_u is the horizontal distance from the hill crest to the upstream slope at 1/2 of the hill height.
AIJ 2004 [27]	$S = (C_1 - 1)\left[C_2\left(\frac{Z}{H_S} - C_3\right) + 1\right] \cdot \exp\left[-C_2\left(\frac{Z}{H_S} - C_3\right)\right] + 1$	H_s is the hill height, and C_1, C_2, and C_3 are coefficients.

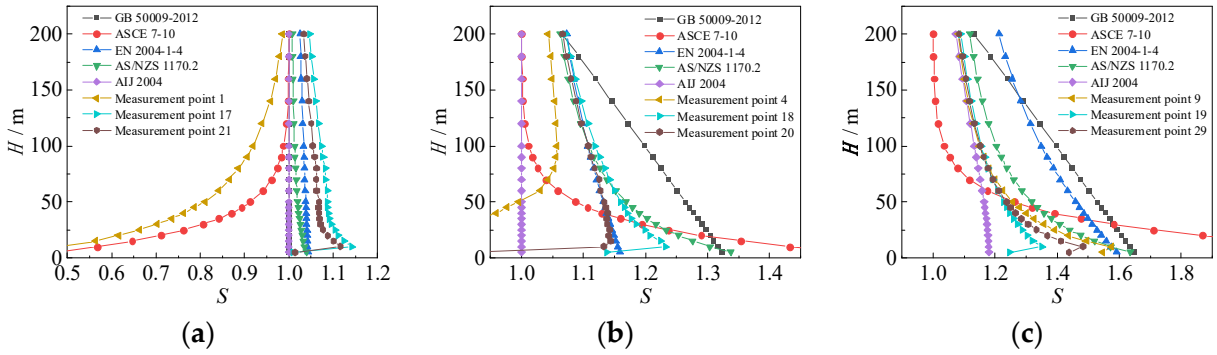


Figure 19. Comparison of the wind speed acceleration ratios in this paper with various codes [23–27]. (**a**) At the foot of the hill. (**b**) At the mid-height of the hill. (**c**) At the top of the hill.

4.5. The Suggestion of Wind Speed Acceleration Ratio

To facilitate the application of the wind speed acceleration ratio results for V-shaped hills in structural design, this study selects the maximum acceleration ratios from all measurement points at the hill's base, midpoint, and top across various wind angles. These values were used to derive formulas for computing the recommended wind acceleration ratio for V-shaped hills under all wind directions, as presented below. To demonstrate the accuracy of the fitting, the wind speed acceleration ratios obtained from the simulation are compared with those computed using the fitted formula, revealing the formula's adeptness in representing the simulation results (Figure 20).

Hill top:

$$S = 134.205 - 73.644\left(\frac{z}{H}\right)^{0.36} - 132.52\cos^{-0.001}(\beta) + 73.181\left(\frac{z}{H}\right)^{0.36}\cos^{-0.001}(\beta) \quad (9)$$

Mid-height of the hill:

$$S = 24.605 - 15.35\left(\frac{z}{H}\right)^{-0.232} - 24.352\cos^{-0.003}(\beta) + 16.332\left(\frac{z}{H}\right)^{-0.232}\cos^{-0.003}(\beta) \quad (10)$$

Foot of the hill:

$$S = 17.376 - 12.116\left(\frac{z}{H}\right)^{-0.083} - 19.055\cos^{-0.006}(\beta) + 15.036\left(\frac{z}{H}\right)^{-0.083}\cos^{-0.006}(\beta) \quad (11)$$

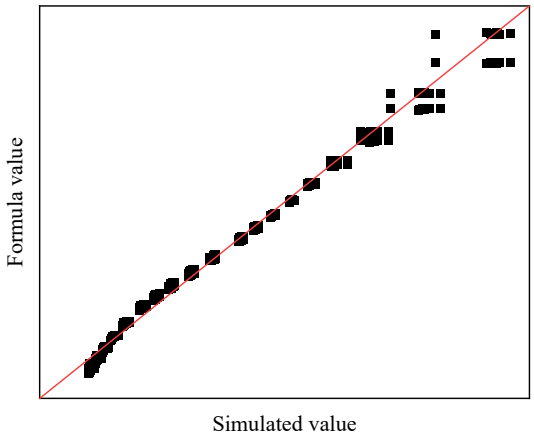


Figure 20. Comparison of formula results and simulation results.

5. Conclusions

This study simulated the wind field of a V-shaped hill using the CFD method. The study examined the impact of wind angle, hill pinch angle, and the distance between the hills on the wind field of the V-shaped hill. The analysis includes the wind speed acceleration at the foot, mid-height, and top of the hill, which were compared with national codes. The following conclusions can be drawn:

(1) The wind speed at the hill's top under various wind angles significantly exceeds that of surrounding areas, resulting in the formation of a wake area behind the V-shaped hill. Beyond a height of 200 m, the wind speed becomes independent of both the topography and wind angle. Generally, the acceleration ratio at the hill's top demonstrates a declining trend as height increases.

(2) At a wind angle of 15°, the V-shaped hill generates a wake zone behind it; moreover, when the pinch angle equals or exceeds 15°, the wake zone gradually transitions from two to one. The acceleration ratios at various locations at the hill's base do not consistently change with height as the angle between the hills varies.

(3) When subjected to oblique wind direction, the V-shaped hill forms a wake zone behind each of the two hills. Moreover, when the distance between the hills equals or exceeds 50 m, the wake zone gradually transitions from a single zone to two distinct zones. The spacing between hills minimally influences the acceleration ratio at both the mid-height and the top of the hill.

(4) The specification of acceleration effects in hilly terrain varies across different codes. At the foot of the hill, the American code indicates the smallest acceleration ratio, which aligns closely with the results presented in this paper. Above 100 m, the American code yields the smallest ratio, while the Chinese code demonstrates the largest ratio below 100 m. The findings in this paper fall within the range of results obtained from the Japanese and Australian codes.

Author Contributions: Conceptualization, J.Y. and Z.T.; methodology, J.Y., Z.T. and H.X.; investigation, J.Y. and Z.T.; writing—original draft preparation, J.Y.; writing—review and editing, Z.T. and H.X. All authors have read and agreed to the published version of the manuscript.

Funding: This research was funded by the the National Natural Science Foundation of China under Grant No. 51978614. The authors also appreciate the strong support of the Nanxun Scholars Program for Young Scholars of ZJWEU under Grant RC2022020946. The opinions and statements do not necessarily represent those of the sponsors.

Institutional Review Board Statement: Not applicable.

Informed Consent Statement: Not applicable.

Data Availability Statement: Data are contained within the article.

Conflicts of Interest: Author Jianfeng Yao was employed by the company Energy Engineering Group Zhejiang Power Design Institute Co., Ltd. The remaining authors declare that the research was conducted in the absence of any commercial or financial relationships that could be construed as a potential conflict of interest.

References

1. Chen, Q.; Yu, C.; Li, Y.; Zhang, X.; He, P. Directional wind characteristics analysis in the mountainous area based on field measurement. *J. Wind Eng. Ind. Aerodyn.* **2022**, *229*, 105162. [CrossRef]
2. Zou, Q.; Li, Z.; Zou, F.; Zeng, X.; Wang, C.; Pan, Y. A study on the characteristics of roof wind field by wind tunnel test. *J. Build. Eng.* **2021**, *43*, 103155. [CrossRef]
3. Song, J.L.; Li, J.W.; Xu, R.Z.; Flay, R.G. Field measurements and CFD simulations of wind characteristics at the Yellow River bridge site in a converging-channel terrain. *Eng. Appl. Comput. Fluid Mech.* **2022**, *16*, 58–72. [CrossRef]
4. Jackson, P.S.; Hunt, J.C.R. Turbulent wind flow over a low hill. *Q. J. R. Meteorol. Soc.* **1975**, *101*, 929–955. [CrossRef]
5. Neff, D.E.; Meroney, R.N. Wind-tunnel modeling of hill and vegetation influence on wind power availability. *J. Wind. Eng. Ind. Aerodyn.* **1998**, *74–76*, 335–343. [CrossRef]
6. Ishihara, T.; Hibi, K.; Oikawa, S. A wind tunnel study of turbulent flow over a three-dimensional steep hill. *J. Wind. Eng. Ind. Aerodyn.* **1999**, *83*, 95–107. [CrossRef]
7. Lubitz, W.D.; White, B.R. Wind-tunnel and field investigation of the effect of local wind direction on speed-up over hills. *J. Wind. Eng. Ind. Aerodyn.* **2007**, *95*, 639–661. [CrossRef]
8. Li, Z.L.; Sun, Y.; Wei, Q.K.; Chen, S. Numerical simulation of mean velocity speed-up effect in Hilly terrain. *Eng. Mech.* **2010**, *27*, 32–37.
9. Song, J.L.; Li, J.W.; Flay, R.G.; Pirooz, A.A.S.; Fu, J.Y. Validation and application of pressure-driven RANS approach for wind parameter predictions in mountainous terrain. *J. Wind. Eng. Ind. Aerodyn.* **2023**, *240*, 105483. [CrossRef]
10. Miller, C.A.; Davenport, A.G. Guidelines for the calculation of wind speed-ups in complex terrain. *J. Wind. Eng. Ind. Aerodyn.* **1998**, *74–76*, 189–197. [CrossRef]
11. Carpenter, P.; Locke, N. Investigation of wind speeds over multiple twodimensional hills. *J. Wind. Eng. Ind. Aerodyn.* **1999**, *83*, 109–120. [CrossRef]
12. Breuer, M.; Peller, N.; Rapp, C.; Manhart, M. Flow over periodic hills – Numerical and experimental study in a wide range of Reynolds numbers. *Comput. Fluids* **2009**, *38*, 433–457. [CrossRef]
13. Li, Z.; Wei, Q.; Sun, Y. Experimental research on amplitude characteristics of complex hilly terrain wind field. *Eng. Mech.* **2012**, *29*, 184–191.
14. Shen, G.H.; Yao, D.; Yu, S.C.; Lou, W.J.; Xing, Y.L. Wind tunnel test of wind field characteristics on isolated hill and two adjacent hills. *J. Zhejiang Univ. (Eng. Sci.)* **2016**, *50*, 812.
15. Li, Z.-H.; Lou, W.-J.; Zhang, L.-G.; Bian, R. Numerical simulation of effects of topographic factors on wind speed in col. *J. Zhejiang Univ. (Eng. Sci.)* **2016**, *50*, 848–855.
16. Lou, W.; Liu, M.; Li, Z.; Zhang, L.; Bian, R. Research on mean wind speed characteristics and speed-up effect in canyon terrain. *J. Hunan Univ. (Nat. Sci.)* **2016**, *43*, 8–15.
17. Turnipseed, A.A.; Anderson, D.E.; Burns, S.; Blanken, P.D.; Monson, R.K. Airflows and turbulent flux measurements in mountainous terrain Part2: Mesoscale effects. *Agric. For. Meteorol.* **2004**, *125*, 187–205. [CrossRef]
18. Bai, H.; Li, J.; Liu, J. Experimental study on wind field characteristics of Sanshui river bridge site located in west valley region. *J. Vib. Shock.* **2012**, *31*, 74–78.
19. Jubayer, C.M.; Hangan, H. A hybrid approach for evaluating wind flow over a complex terrain. *J. Wind. Eng. Ind. Aerodyn.* **2018**, *175*, 65–76. [CrossRef]
20. Yu, C.; Li, Y.; Zhang, M.; Zhang, Y.; Zhai, G. Wind characteristics along a bridge catwalk in a deep-cutting gorge from field measurements. *J. Wind. Eng. Ind. Aerodyn.* **2019**, *186*, 94–104. [CrossRef]
21. Yang, Q.; Zhou, T.; Yan, B.; Liu, M.; Van Phuc, P.; Shu, Z. LES study of topographical effects of simplified 3D hills with different slopes on ABL flows considering terrain exposure conditions. *J. Wind. Eng. Ind. Aerodyn.* **2021**, *210*, 104513. [CrossRef]
22. Cheng, X.; Yan, B.; Zhou, X.; Yang, Q.; Huang, G.; Su, Y.; Yang, W.; Jiang, Y. Wind resource assessment at mountainous wind farm: Fusion of RANS and vertical multi-point on-site measured wind field data. *Appl. Energy* **2024**, *363*, 123116. [CrossRef]
23. *GB 50009-2012*; Load Code for the Design of Building Structures. Architecture and Building Press: Beijing, China, 2012.
24. *ASCE 7-10*; Minimum Design Loads for Buildings and Other Structures. ASCE: New York, NY, USA, 2010.
25. *EN 2004-1-4*; Actions on Structures; European standard. European Committee for Standardization: Brussels, Belgium, 2004.
26. *AS/NZS 1170.0*; Structural design actions, Part 2: Wind actions. Australian/New Zealand Standard. Standards Australia: Sydney, NSW, Australia; Standards New Zealand: Wellington, New Zealand, 2011.
27. Architectural Institute of Japan. *AIJ Recommendations for Loads on Buildings*; Architectural Institute of Japan: Tokyo, Japan, 2004.

Disclaimer/Publisher's Note: The statements, opinions and data contained in all publications are solely those of the individual author(s) and contributor(s) and not of MDPI and/or the editor(s). MDPI and/or the editor(s) disclaim responsibility for any injury to people or property resulting from any ideas, methods, instructions or products referred to in the content.